

Wave propagation in high-contrast media: periodic and beyond*

Élise Fressart[†] Barbara Verfürth[‡]

Abstract. This work is concerned with the classical wave equation with a high-contrast coefficient in the spatial derivative operator. We first treat the periodic case, where we derive a new limit in the one-dimensional case. The behavior is illustrated numerically and contrasted to the higher-dimensional case. For general unstructured high-contrast coefficients, we present the Localized Orthogonal Decomposition and show a priori error estimates in suitably weighted norms. Numerical experiments illustrate the convergence rates in various settings.

Key words. Multiscale method, homogenization, wave propagation, high-contrast material

AMS subject classifications. 65M15, 65M12, 35B27, 35L05, 78M40

1 Introduction

The classical wave equation is a popular prototypical model to study the propagation of various types of waves, e.g., in acoustics or electromagnetics. In the avenue of modern metamaterials, the study of wave propagation through heterogeneous, or even more precisely, multiscale materials receives a lot of interest. In such media, the properties of the material vary on short spatial scales, for instance, because the material is a composite with fine-scale features. The material properties of the, for simplicity, two components can be of very different magnitude leading to a *high contrast* in the material properties over the whole metamaterial bulk. Mathematically, this is often modeled by coupling the contrast in the PDE coefficients to the fine-scale parameter ϵ , which originally describes the length scale on which the coefficients variations occur.

Such a high contrast is known to produce interesting wave propagation phenomena, which also have been investigated mathematically, often with the help of asymptotic analysis. An incomplete list (focusing on mathematical contributions) includes Helmholtz resonators [17], artificial magnetism [8], and negative refraction [16]. We also refer to the overviews [27] and [5] and references therein. Most of these works consider *time-harmonic* wave propagation. Inspired by the analytical results, the numerical homogenization of time-harmonic waves in high-contrast media has been addressed with the Heterogeneous Multiscale Method in [23, 22, 28] and with the Localized Orthogonal Decomposition (LOD) in [26].

*Funded by the Deutsche Forschungsgemeinschaft (DFG, German Research Foundation) under VE 1397/2-1. Major parts of this work were accomplished while BV was affiliated with Karlsruher Institut für Technologie (KIT) and EF conducted a research internship at KIT. The work of BV at University Bonn is also funded by the Deutsche Forschungsgemeinschaft (DFG, German Research Foundation) under Germany's Excellence Strategy – EXC-2047/1 – 390685813.

[‡]Institut für Numerische Simulation, Universität Bonn, Friedrich-Hirzebruch-Allee 7, D-53115 Bonn, Germany

[†]École Nationale des Ponts et Chaussées (ENPC), 6 et 8 Avenue Blaise Pascal, 77455 Marne-la-Vallée cedex 2, France

On the other hand, the time-domain wave equation in multiscale materials with *low contrast* is also well studied. Asymptotic analysis results date back to [7]. Numerical multiscale methods for the wave equation are reviewed in [2]. Focusing on unstructured coefficients with a continuum of scales, rough polyharmonic splines were used in [24] and the LOD in [1]. The LOD has then been combined with explicit time stepping [19], mass lumping [12] and time-dependent coefficients [26]. We refer to [4, 20] for further applications of the LOD besides the classical wave equation.

Motivated by these results, we aim to (numerically) study the *time-domain wave equation in a high-contrast material*. Specifically, we assume the coefficient in the spatial derivative of the wave equation to take the values 1 or ϵ^2 . The exact scaling of the high contrast is motivated by the fact that this choice has turned out to result in unusual limit equations in the time-harmonic [8] as well as the time-domain setting [21]. Our study can roughly be divided into two parts. In the first part, we consider an ϵ -periodic material. Asymptotic analysis results show a significant difference between one and higher space dimensions. We provide a new limit characterization in the one-dimensional setting, which gives an explicit and simple formula for the homogenized solution in case of vanishing right-hand side. The higher-dimensional setting has been treated in [21] in detail and we briefly review the main findings. Direct numerical simulations illustrate the differences and connections between the low- and high-contrast as well as the one- and the two-dimensional case. In the second part of our study, we consider a general unstructured high-contrast material. We use the LOD for the wave equation in [1] combined with specific interpolation operators designed for stationary high-contrast problems in [15, 25, 26]. The main contribution consists in a priori error estimates for the semi-discrete method in the high-contrast case. The extension from stationary to time-dependent problems turns out to be non-trivial, in particular because of the necessity to work with weighted spatial norms. We carefully discuss the ϵ -dependence of our bounds. Several numerical experiments underline the applicability of the approach in one- as well as two-dimensional settings, even for unstructured coefficients. Overall, we hope to showcase the analytical and numerical implications of wave propagation in high-contrast media and to inspire further research on the topic.

The paper is organized as follows. In Section 2, we describe the considered settings in detail. Section 3 contains the first part of our study, namely the periodic setting with asymptotic analysis results and associated numerical illustrations. The second part of our study concerning the numerical multiscale method beyond the periodic case is contained in Section 4. Finally, we draw some conclusions and point out open questions.

2 Setting

Throughout this article, we use standard notation on Lebesgue, Sobolev, and Bochner spaces. Scalar products are denoted by (\cdot, \cdot) with an index specifying the Hilbert space (mostly L^2) and by $\langle \cdot, \cdot \rangle$, we denote the duality pairing between H^{-1} and H_0^1 . $\Omega \subset \mathbb{R}^d$ denotes the open, connected Lipschitz (spatial) domain and $[0, T]$ the time domain with final time T .

We consider the following wave equation

$$\begin{cases} \partial_{tt}u_\epsilon - \nabla \cdot (a_\epsilon(x)\nabla u_\epsilon) &= f & \text{in } \Omega \times (0, T], \\ u_\epsilon(x, t) &= 0 & \text{on } \partial\Omega \times [0, T], \\ u_\epsilon(x, 0) &= u^0(x), \\ \partial_t u_\epsilon(x, 0) &= v^0(x). \end{cases} \quad (2.1)$$

with source term $f \in L^2(0, T, L^2(\Omega))$ and initial values $u^0 \in H_0^1(\Omega)$ and $v^0 \in L^2(\Omega)$. We assume

that $a_\epsilon \in L^\infty(\Omega)$ takes only two values, precisely

$$a_\epsilon = \begin{cases} a_0 & \text{in } \Omega_\epsilon, \\ 1 & \text{else,} \end{cases} \quad (2.2)$$

for some positive constant $a_0 > 0$. The subscript ϵ indicates multiscale features, i.e., we implicitly assume that Ω_ϵ consists of $\mathcal{O}(\epsilon^{-d})$ connected components with diameter $\mathcal{O}(\epsilon)$. More detailed assumptions on a_ϵ will be specified in each section.

It is well known that under the above assumptions, there exists a unique weak solution to (2.1), i.e., there exists a unique $u_\epsilon \in L^2(0, T, H_0^1(\Omega))$ with $\partial_t u_\epsilon \in L^2(0, T, L^2(\Omega))$ and $\partial_{tt} u_\epsilon \in L^2(0, T, H^{-1}(\Omega))$ such that

$$\begin{cases} \langle \partial_{tt} u_\epsilon, v \rangle + (a_\epsilon \nabla u_\epsilon, \nabla v)_{L^2(\Omega)} = (f, v)_{L^2(\Omega)} & \forall v \in H_0^1(\Omega), \text{ for a.e. } t \in [0, T], \\ u_\epsilon(\cdot, 0) = u^0, \\ \partial_t u_\epsilon(\cdot, 0) = v^0. \end{cases} \quad (2.3)$$

We introduce the notation $b_\epsilon(v, w) = \int_\Omega a_\epsilon \nabla v \cdot \nabla w$ for all $v, w \in H_0^1(\Omega)$.

The goal is to compare the behavior of u_ϵ for the *low contrast* case with $a_0 = \mathcal{O}(1)$ and the *high contrast* one with $a_0 = \mathcal{O}(\epsilon^2)$. In particular we emphasize that b_ϵ is almost degenerate in the high contrast case in the sense that its coercivity constant tends to zero for $\epsilon \rightarrow 0$. One could also consider other ϵ -scalings of a_0 . However, we restrict our studies to this specific setting as it turned out to show interesting resonances in the time-harmonic case. Let us emphasize at this point that we only consider final times $T = \mathcal{O}(1)$ and thereby avoid any considerations of additional long-time effects.

3 Asymptotic results in the periodic case

The periodic case is specified via the (periodic) form of Ω_ϵ which we define as

$$\Omega_\epsilon = \left(\bigcup_{j \in \mathbb{Z}^d} \epsilon(j + \Sigma) \right) \cap \Omega$$

for a subdomain $\Sigma \subset Y := (0, 1)^d$. We call Y the unit cell and Σ the inclusion. For $d = 1$, we only assume that Σ is a true subdomain, i.e., unequal to Y . For $d \geq 2$, we assume that Σ is compactly embedded in Y , i.e., it does not touch the boundary of Y . This prevents high contrast features to run through the whole domain Ω .

In the low contrast setting, the limit $\epsilon \rightarrow 0$ is well studied using homogenization theory. We have the following result for the solution u_ϵ to (2.3), cf. [1, 2, 7]. It holds

$$\begin{aligned} u_\epsilon &\rightharpoonup \hat{u} && \text{weakly-* in } L^\infty(0, T, H_0^1(\Omega)) \\ \partial_t u_\epsilon &\rightharpoonup \partial_t \hat{u} && \text{weakly-* in } L^\infty(0, T, L^2(\Omega)) \end{aligned}$$

where $\hat{u} \in L^2(0, T, H_0^1(\Omega))$, $\partial_t \hat{u} \in L^2(0, T, L^2(\Omega))$, $\partial_{tt} \hat{u} \in L^2(0, T, H^{-1}(\Omega))$ and \hat{u} is the solution of the homogenized problem

$$\begin{cases} \langle \partial_{tt} \hat{u}, v \rangle + (\hat{a} \nabla \hat{u}, \nabla v)_{L^2(\Omega)} = (f, v)_{L^2(\Omega)} & \forall v \in H_0^1(\Omega) \text{ and a.e. } t \in [0, T] \\ \hat{u}(\cdot, 0) = u^0 \\ \partial_t \hat{u}(\cdot, 0) = v^0 \end{cases} \quad (3.1)$$

Especially in the periodic case, details on the homogenized coefficient \hat{a} are available. They are presented depending on the space dimension in Section 3.1 and Section 3.2, respectively, where we also discuss results for the high-contrast case. Numerical illustrations in Section 3.3 complement the theoretical results and showcase the different behavior in one and two space dimensions.

3.1 One-dimensional case

In the one-dimensional case, \hat{a} in (3.1) takes a simple form, namely the harmonic average, i.e.,

$$\hat{a} = \left(\int_0^\epsilon \frac{1}{a_\epsilon} dx \right)^{-1}.$$

Using the even more specific definition of a_ϵ in (2.2), we obtain

$$\hat{a} = \left(\frac{|\Sigma|}{a_0} + 1 - |\Sigma| \right)^{-1} = \frac{a_0}{a_0 + (1 - a_0)|\Sigma|}, \quad (3.2)$$

where $|\Sigma|$ denotes the length of the subinterval Σ .

In the high-contrast case, we have the following asymptotic result.

Proposition 3.1. *Let $d = 1$, $\epsilon \leq 1$ and let u_ϵ be the solution to (2.3) with $a_0 = \epsilon^2$, Ω_ϵ as specified above, $f \equiv 0$ and initial values $u^0, v^0 \in H_0^1(\Omega)$. Then there is $\hat{u} \in L^2(0, T, H_0^1(\Omega))$ with $\partial_t \hat{u} \in L^2(0, T, L^2(\Omega))$ such that u_ϵ two-scale converges to \hat{u} as $\epsilon \rightarrow 0$. \hat{u} is explicitly given as*

$$\hat{u}(x, t) = u^0(x) + v^0(x)t.$$

Note that, formally, we would get $\hat{a} \rightarrow 0$ for $\epsilon \rightarrow 0$ which agrees with the above formula for \hat{u} .

Proof. Since $f \equiv 0$ we have conservation of the energy

$$E(t)^2 := \frac{1}{2} \|\partial_t u_\epsilon(\cdot, t)\|_{L^2(\Omega)}^2 + \frac{1}{2} \|\sqrt{a_\epsilon} \nabla u_\epsilon(\cdot, t)\|_{L^2(\Omega)}^2,$$

i.e., $E(t) = E(0)$ for all t . By the assumptions on u^0, v^0 and a_ϵ , $E(0)$ is uniformly bounded in ϵ for $\epsilon \leq 1$. This implies that

$$\|\partial_t u_\epsilon\|_{L^\infty(0, T, L^2(\Omega))} < C, \quad \epsilon \|\nabla u_\epsilon\|_{L^\infty(0, T, L^2(\Omega))} < C, \quad \|\nabla u_\epsilon\|_{L^\infty(0, T, L^2(\Omega \setminus \Omega_\epsilon))} < C$$

with constants C independent of ϵ . Standard energy-type estimates for the wave equation further yield that

$$\|u_\epsilon\|_{L^\infty(0, T, L^2(\Omega))} < C$$

with a constant C only depending on the initial values and thus independent of ϵ . Note that since T is finite, we get similar estimates as the four above also for L^2 -norms with respect to time instead of L^∞ -norms.

Using the arguments from the stationary case in [10, Appendix A] and treating t as a parameter, we see that there exists $\bar{u} \in L^2((0, T) \times \Omega, V_1)$ such that — up to a subsequence —

- u_ϵ two-scale converges to \bar{u} ,
- $\epsilon \nabla u_\epsilon$ two-scale converges to $\nabla_y \bar{u}$,
- $\chi_{\Omega \setminus \Omega_\epsilon} \nabla u_\epsilon$ two-scale converges to zero.

Here, χ_A denotes the characteristic function of the set A and we define the space $V_1 := \{v \in H_{\#}^1(Y) : \nabla_y v = 0 \text{ in } Y \setminus \bar{\Sigma}\}$, where the subscript $\#$ indicates periodic function spaces. By the boundedness of $\partial_t u_\epsilon$ and the two-scale convergence of u_ϵ , we in fact get, cf. [21], that $\partial_t \bar{u} \in L^2((0, T) \times \Omega \times Y)$ and $\partial_t u_\epsilon$ two-scale converges to $\partial_t \bar{u}$.

With these convergences and choosing a test function of the form $v(x, x/\epsilon)$ with $v \in C_c^\infty(\Omega, V_1)$, we can pass to the limit in (2.3). The second time derivative of u_ϵ and the initial conditions can be treated as discussed in detail in [21, Sec. 3]. We get the limit system

$$\langle \partial_{tt}\bar{u}, \psi \rangle_{\Omega \times Y} + (\nabla_y \bar{u}, \nabla_y \psi)_{L^2(\Omega \times \Sigma)} = 0 \quad \forall \psi \in L^2(\Omega, V_1)$$

with the initial conditions $\bar{u}(x, y, 0) dx = u^0(x)$ and $\partial_t \bar{u}(x, y, 0) dy = v^0(x)$. Note that the result so far only holds for a subsequence. But since the solution \bar{u} is unique by energy arguments, the result then holds for the whole sequence.

The dependence on x in this limit equation is only parametric. In other words, we can write $\bar{u}(x, y, t) = u^0(x)w_1(y, t) + v^0(x)w_2(y, t)$, where $w_i(\cdot, t) \in V_1$ solves

$$\langle \partial_{tt}w_i, \psi \rangle_Y + (\nabla_y w_i, \nabla_y \psi)_\Sigma = 0 \quad \forall \psi \in V_1$$

with the initial conditions $w_i(\cdot, 0) = \delta_{i1}$ and $\partial_t w_i(\cdot, 0) = \delta_{i2}$ with the Kronecker delta. A standard energy argument shows that the solutions w_1 and w_2 are unique. As one easily sees, we have $w_1 \equiv 1$ and $w_2(y, t) = t$ as solutions, which finishes the proof. \square

3.2 Changes in higher dimensions

In higher space dimensions, homogenization results are more involved. In the low-contrast case, the formula for \hat{a} involves the solution of additional PDEs on the unit cell Y . As in the stationary case one has [7]

$$(\hat{a})_{ij} = \int_Y a(e_i + \nabla_y \xi_i) \cdot (e_j + \nabla_y \xi_j) dy, \quad i, j = 1, \dots, d, \quad (3.3)$$

where e_i are the canonical basis vectors of \mathbb{R}^d and a is the Y -periodic function such that $a_\epsilon = a(x/\epsilon)$. Further, ξ_i , $i = 1, \dots, d$, is the unique Y -periodic H^1 -function with zero mean, written as $\xi_i \in H_{\#,0}^1(Y)$, that solves the so-called cell problem

$$\int_Y a(e_i + \nabla_y \xi_i) \cdot \nabla_y v = 0 \quad \text{for all } v \in H_{\#,0}^1(Y). \quad (3.4)$$

Note that even though we assumed a_ϵ to be scalar-valued, the homogenized coefficient \hat{a} is matrix-valued in general. Moreover, even in our configuration (2.2) for a_ϵ , we can no longer give a closed formula for \hat{a} .

The results become even more intricate for the high contrast case with $a_0 = \epsilon^2$ in (2.3). According to [21], u_ϵ two-scale converges to $\hat{u}(x, t) + \tilde{u}(x, y, t)$, where $\hat{u} \in L^\infty(0, T, H_0^1(\Omega))$ with $\partial_t \hat{u} \in L^\infty(0, T, L^2(\Omega))$, $\partial_{tt} \hat{u} \in L^\infty(0, T, H^{-1}(\Omega))$ and $\tilde{u} \in L^2((0, T) \times \Omega, H_0^1(\Sigma))$ with $\partial_t \tilde{u} \in L^2((0, T) \times \Omega \times \Sigma)$, $\partial_{tt} \tilde{u} \in L^2((0, T) \times \Omega, H^{-1}(\Sigma))$. The pair (\hat{u}, \tilde{u}) is the unique solution to

$$\langle \partial_{tt} \hat{u} + \partial_{tt} \tilde{u}, \psi + \psi_1 \rangle_{\Omega \times \Sigma} + (\hat{a} \nabla \hat{u}, \nabla \psi)_{L^2(\Omega)} + (a \nabla_y \tilde{u}, \nabla_y \psi_1)_{L^2(\Omega \times \Sigma)} = (f, \psi)_\Omega \quad (3.5)$$

for all $(\psi, \psi_1) \in H_0^1(\Omega) \times L^2(\Omega, H_0^1(\Sigma))$ and almost all $t \in [0, T]$ with the initial conditions

$$\begin{cases} \hat{u}(\cdot, 0) &= (1 - |\Sigma|)u^0, & \tilde{u}(\cdot, \cdot, 0) &= |\Sigma|u^0 \\ \partial_t \hat{u}(\cdot, 0) &= (1 - |\Sigma|)v^0, & \partial_t \tilde{u}(\cdot, \cdot, 0) &= |\Sigma|v^0 \end{cases} \quad (3.6)$$

Here, \hat{a} is defined similar to (3.3)–(3.4), but the cell problems and the integration only occur in $Y \setminus \bar{\Sigma}$. This is a coupled system for \hat{u} and \tilde{u} and, as [21] explains, it remains unclear whether or how it can be decoupled into a truly homogenized system for \hat{u} alone with an (additional)

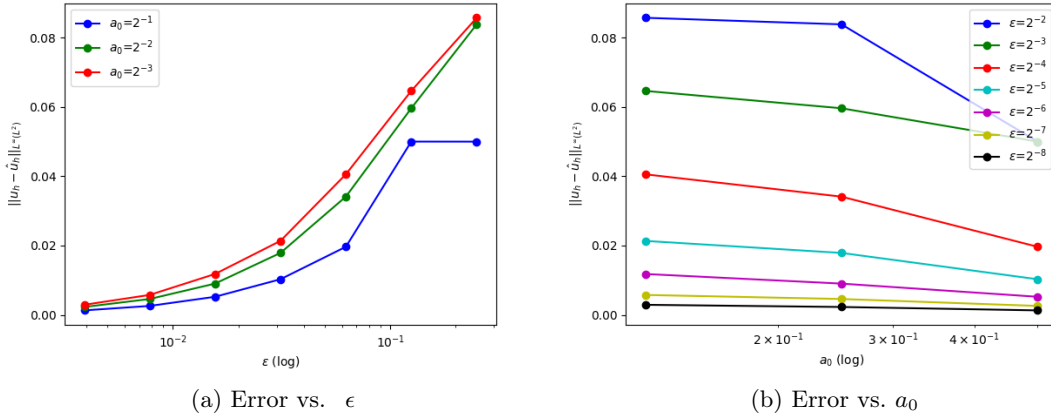


Figure 3.1: Homogenization error in $L^\infty(0, T, L^2(\Omega))$ -norm for different values of a_0 and ϵ

homogenized coefficient derived from \tilde{u} . In other words, when setting $\psi \equiv 0$ in (3.5), we cannot solve the resulting problem for \tilde{u} depending only on \hat{u} , since $\partial_{tt}\hat{u}$ still appears. This is strikingly different from the stationary high-contrast case, where an additional homogenized coefficient arises, cf. [3]. Moreover, the system cannot be decoupled even in the case $f \equiv 0$. In particular, a more complex behavior of the homogenized solution \hat{u} is expected in higher space dimensions than in the one-dimensional case discussed above.

3.3 Numerical illustrations

In the following, we illustrate the differences between low- and high-contrast settings and one- versus two-dimensional settings by (direct) numerical simulations of (2.3). We use linear finite elements on a mesh resolving the periodicity of a_ϵ and the implicit mid-point rule for time stepping. Experiments were conducted in `python` using the module `scikit-fem` [13] for the finite element stiffness and mass matrices.

First, we investigate the homogenization error in the one-dimensional setting depending on ϵ and the choice of a_0 . For this, we numerically compute u_ϵ as solution to (2.3) and \hat{u} as solution to (3.1) and consider their difference in the $L^\infty(0, T, L^2(\Omega))$ -norm. Let $\Omega = (0, 1)$ and $T = 0.25$. We use a uniform grid with resolution $h = 2^{-13}$ and the time step size $\tau = 2^{-9}$. We consider $f = 0$, $u^0(x) = \exp(-\frac{(x-0.5)^2}{\sigma^2})$ with $\sigma = 0.1$, and $v^0 = 0$. We choose an ϵ -periodic coefficient taking the values 1 or a_0 , i.e.,

$$a_\epsilon(x) = a\left(\frac{x}{\epsilon}\right) \quad \text{with} \quad a(y) = \begin{cases} a_0 & \text{if } \frac{1}{4} < y \leq \frac{3}{4} \\ 1 & \text{if } 0 < y \leq \frac{1}{4} \text{ or } \frac{3}{4} < y \leq 1 \end{cases}$$

As expected, the homogenization error $u_\epsilon - \hat{u}$ decreases with decreasing ϵ until the temporal and spatial discretization errors dominate, see Figure 3.1a. This behavior seems rather independent from the chosen value of a_0 , but note that the depicted values still entail a somewhat moderate contrast in a_ϵ . To investigate this further, we depict the homogenization error in dependence of a_0 for different ϵ in Figure 3.1b. For fixed ϵ , the considered error slightly increases when a_0 decreases. Figure 3.1 is in line with the formal observation above that the formula (3.2) for \hat{a} tends to 0 for $a_0 \rightarrow 0$ and thereby formally coincides with the asymptotic result in the high contrast setting from Proposition 3.1. We may conclude that in 1d, \hat{a} from (3.2) seems to give a good homogenization formula in the low- as well as the high-contrast setting.

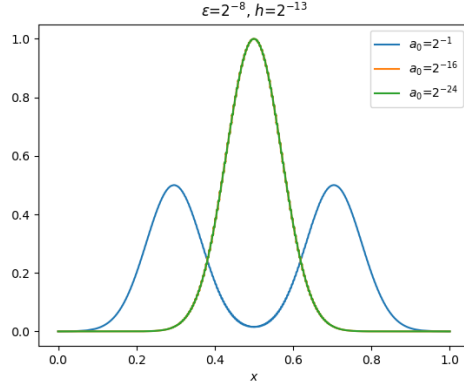


Figure 3.2: Solutions for $\epsilon = 2^{-8}$ and different values of a_0 at time $T = 0.25$

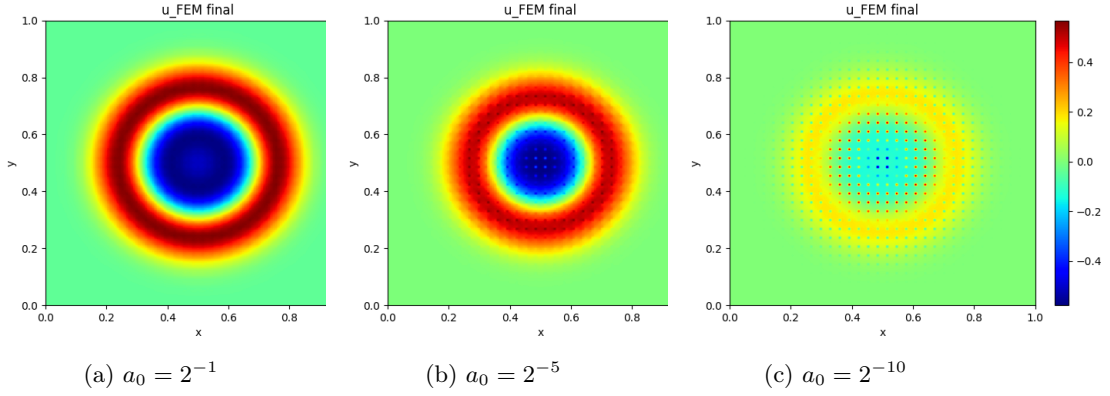


Figure 3.3: Solutions for different values of a_0 with $\epsilon = 2^{-5}$

Second, we aim to illustrate the findings of Proposition 3.1 more. Precisely, we contrast the behavior of u_ϵ for different choices of a_0 in Figure 3.2 for $T = 0.25$. We use the same setting as in the previous paragraph. The orange line, which lies on top of the green one, corresponds to the high-contrast case $a_0 = \epsilon^2$ studied in Proposition 3.1. In fact, u_ϵ does not seem to move, or in other words, it is very close to the initial value. This should be contrasted with the moving pulse (in blue) for the low contrast case. Figure 3.2 suggests that the limit formula from Proposition 3.1 may also hold for other scalings of a_0 , namely $a_0 = \epsilon^p$ with $p \geq 2$, since the green curve corresponds to $p = 3$.

Third, we aim to illustrate that the high-contrast behavior described in the previous paragraph and justified theoretically via Proposition 3.1 is specific to the one-dimensional setting. Therefore, we now consider the two-dimensional case, where Section 3.2 predicts a more complex (limit) behavior. We choose $\Omega = (0, 1)^2$ and $T = 0.25$. We consider $h = 2^{-7}$, $\tau = 2^{-9}$, $f = 0$, $u^0(x, y) = \exp(-\frac{(x-0.5)^2}{\sigma^2} - \frac{(y-0.5)^2}{\sigma^2})$ with $\sigma = 0.1$, and $v^0 = 0$. The coefficient a_ϵ is set as follows

$$a_\epsilon(x) = a\left(\frac{x}{\epsilon}\right) \quad \text{with} \quad a(y) = \begin{cases} a_0 & \text{if } y \in \left(\frac{1}{4}, \frac{3}{4}\right)^2 \\ 1 & \text{if } y \in (0, 1)^2 \setminus \left(\frac{1}{4}, \frac{3}{4}\right)^2 \end{cases}$$

We call inclusions the parts of the domain where $a_\epsilon = a_0$. The amplitude of the solution is

greater inside the inclusions (see Figure 3.3). For fixed ϵ , the difference of amplitudes between the inclusions and the rest of the domain is more and more visible when a_0 decreases. In contrast to the one-dimensional setting, the wave still propagates notably in the high-contrast case.

4 Numerical approach beyond periodicity

In this section, we drop the assumption on the periodic set-up of Ω_ϵ . One should still imagine that Ω_ϵ consists of about $O(\epsilon^{-d})$ subdomains of diameter $O(\epsilon)$, but they are not necessarily arranged in a periodic fashion. We present and analyze a numerical (multiscale) method that provides an approximation of u_ϵ on a coarse scale $H \gg \epsilon$ in Section 4.1. This scale is typically introduced by the (coarse) mesh size of the triangulation. Precisely, our approach relies on the Localized Orthogonal Decomposition (LOD), which was studied for the low-contrast case in [1]. In the stationary as well as the time-harmonic setting, the high-contrast case has been covered in [25, 15] and [26], respectively. We will describe the required adaptations of the method, which introduce some implicit assumptions on the structure of Ω_ϵ (at least for the theory). The main goal is the numerical analysis of the LOD for the high-contrast wave equation in Section 4.2, which naturally combines techniques from [1] and [25, 26]. Numerical experiments in Section 4.3 illustrate the results.

4.1 Localized Orthogonal Decomposition

The LOD is a spatial discretization method, which we combine with a standard time stepping scheme. For self-consistency of the material, we briefly review the LOD for the wave equation, closely following the presentation and notation of [1].

Spatial discretization. We introduce a (coarse) rectangular¹ mesh \mathcal{T}_H with mesh size H and a fine rectangular mesh \mathcal{T}_h , where the latter resolves the variations of a_ϵ . All meshes are assumed to be shape-regular (in the sense that the smallest angle is bounded from below), \mathcal{T}_H is also quasi-uniform, and \mathcal{T}_h is a refinement of \mathcal{T}_H . Let $V_H = Q_1(\mathcal{T}_H) \cap H_0^1(\Omega)$ and $V_h = Q_1(\mathcal{T}_h) \cap H_0^1(\Omega)$ be the associated lowest-order finite element spaces, where $Q_1(\mathcal{T}_h)$ is the space of possibly discontinuous functions that are polynomials of coordinate degree at most one on each element of \mathcal{T}_h . Let $I_H : H_0^1(\Omega) \rightarrow V_H$ be a stable interpolation operator. Necessary assumptions on I_H as well as possible choices are discussed further below. Let $W_h = \ker(I_H)$.

The corrector $\mathcal{C}_{h,\Omega} : V_H \rightarrow W_h$ is the solution $\mathcal{C}_{h,\Omega}(v_H) \in W_h$ of

$$(a_\epsilon \nabla \mathcal{C}_{h,\Omega}(v_H), \nabla w_h)_{L^2(\Omega)} = -(a_\epsilon \nabla v_H, \nabla w_h)_{L^2(\Omega)} \quad \text{for all } w_h \in W_h.$$

For a coarse element $K \in \mathcal{T}_H$, a patch $U_m(K)$ is defined as follows

$$\begin{aligned} U_0(K) &= K, \\ U_m(K) &= \bigcup \{T \in \mathcal{T}_H \mid T \cap U_{m-1}(K) \neq \emptyset\}, \quad m \geq 1. \end{aligned} \tag{4.1}$$

We define the space $W_h(U_m(K)) = \{w_h \in W_h \mid w_h = 0 \text{ in } \Omega \setminus U_m(K)\}$ and the localized correctors $\mathcal{C}_{h,m}^K$ as follows : for $v_H \in V_H$, $\mathcal{C}_{h,m}^K(v_H) \in W_h(U_m(K))$ solves

$$\int_{U_m(K)} a_\epsilon \nabla \mathcal{C}_{h,m}^K(v_H) \cdot \nabla w_h = - \int_K a_\epsilon \nabla v_H \cdot \nabla w_h \quad \forall w_h \in W_h(U_m(K)) \tag{4.2}$$

¹Since our implementation is based on rectangular meshes, we restrict the presentation to this case. However, results transfer to general parallelepiped meshes in higher dimensions as well as to simplicial meshes.

Let the global approximation $\mathcal{C}_{h,m}$ of $\mathcal{C}_{h,\Omega}$ be defined by $\mathcal{C}_{h,m}(v_H) = \sum_{K \in \mathcal{T}_H} \mathcal{C}_{h,m}^K(v_H)$. The LOD space is now $V_{H,m}^{ms} = \{v_H + \mathcal{C}_{h,m}(v_H) | v_H \in V_H\}$.

We introduce the following notations

$$\begin{aligned} b_{H,m}(v_H, w_H) &= b_\epsilon(v_H + \mathcal{C}_{h,m}(v_H), w_H + \mathcal{C}_{h,m}(w_H)), \\ (v_H, w_H)_{H,m} &= (v_H + \mathcal{C}_{h,m}(v_H), w_H + \mathcal{C}_{h,m}(w_H))_{L^2(\Omega)} \end{aligned}$$

Let $u_{H,m} \in H^2(0, T, V_H)$ denote the semi-discrete approximation. It solves the following system for almost all $t > 0$ and $v_H \in V_H$

$$\begin{cases} (\partial_{tt} u_{H,m}(\cdot, t), v_H)_{H,m} + b_{H,m}(u_{H,m}(\cdot, t), v_H) &= (f(\cdot, t), v_H + \mathcal{C}_{h,m}(v_H))_{L^2(\Omega)} \\ (u_{H,m} + \mathcal{C}_{h,m}(u_{H,m}))(\cdot, 0) &= \pi_{H,m}^{ms}(u^0) \\ \partial_t (u_{H,m} + \mathcal{C}_{h,m}(u_{H,m}))(\cdot, 0) &= v_{H,m}^0 \end{cases} \quad (4.3)$$

where $\pi_{H,m}^{ms} : H_0^1(\Omega) \rightarrow V_{H,m}^{ms}$ is the elliptic projection on $V_{H,m}^{ms}$. The second initial value $v_{H,m}^0$ can be chosen as either $\pi_{H,m}^{ms}(v^0)$ or as $P_{H,m}^{ms}(v^0)$, where $P_{H,m}^{ms} : H_0^1(\Omega) \rightarrow V_{H,m}^{ms}$ is the L^2 -projection on $V_{H,m}^{ms}$. Besides $u_{H,m}$ we also define the semi-discrete multiscale approximation $u_{H,m}^{ms} \in H^2(0, T, V_{H,m}^{ms})$ via $u_{H,m}^{ms} = (1 + \mathcal{C}_{h,m})u_{H,m}$.

Let \mathcal{N}_H denote the set of the interior vertices of the coarse grid. $\phi_z \in V_H$ denotes the nodal basis function corresponding to the node $z \in \mathcal{N}_H$. N refers to the number of interior coarse nodes. We introduce the corrected stiffness matrix S_m , corrected mass matrix M_m and corrected source vector F_m , respectively, as

$$(S_m)_{i,j} = b_{H,m}(\phi_{z_j}, \phi_{z_i}), \quad (M_m)_{i,j} = (\phi_{z_j}, \phi_{z_i})_{H,m}, \quad (F_m)_i(t) = (f(\cdot, t), \phi_{z_i} + \mathcal{C}_{h,m}(\phi_{z_i}))_{L^2(\Omega)}.$$

The initial vectors $\overline{u_m^0}$ and $\overline{v_m^0}$ are given by

$$(\overline{u_m^0})_i \text{ is such that } \pi_{H,m}^{ms}(u^0) = \sum_{i=1}^N (\overline{u_m^0})_i (\phi_{z_i} + \mathcal{C}_{h,m}(\phi_{z_i})) \quad (4.4)$$

$$(\overline{v_m^0})_i \text{ is such that } v_{H,m}^0 = \sum_{i=1}^N (\overline{v_m^0})_i (\phi_{z_i} + \mathcal{C}_{h,m}(\phi_{z_i})) \quad (4.5)$$

Note that M_m and S_m are time-independent and need to be assembled only once. Expanding $u_{H,m}$ in the basis $(\phi_{z_i})_{1 \leq i \leq N}$, i.e., $u_{H,m}(\cdot, t) = \sum_{i=1}^N (\zeta_m(t))_i \phi_{z_i}$, (4.3) can be written as a system of ODEs for $\zeta_m(t)$.

Time discretization. We can equally use the implicit midpoint rule or the Crank-Nicolson scheme from [1]. In the considered setting, both schemes differ only in the treatment of the right-hand side f and are even equivalent if the time dependency of f is affine. Let τ be the time step size and set $t^n = \tau n$ for $n \in \{0, \dots, J = T/\tau\}$ and, similarly, $t^{n+\frac{1}{2}} = \tau(n + \frac{1}{2})$. We are interested in finding an approximation ζ_m^n for $\zeta_m(t^n)$. To re-write the ODE system of second order for ζ_m in a system of first order, we introduce the auxiliary quantity $\eta_m = \dot{\zeta}_m$. The time-discrete approximations (ζ_m^n, η_m^n) to $(\zeta_m(t^n), \eta_m(t^n))$ are determined via the following system

$$\begin{aligned} \zeta_m^0 &= \overline{u_m^0} \\ \eta_m^0 &= \overline{v_m^0} \\ \left(M_m + \frac{\tau^2}{4} S_m\right) \eta_m^{n+\frac{1}{2}} &= M_m \eta_m^n + \frac{\tau}{2} \left(-S_m \zeta_m^n + M_m F_m^{n+\frac{1}{2}}\right) \\ \zeta_m^{n+1} &= \zeta_m^n + \tau \eta_m^{n+\frac{1}{2}} \\ \eta_m^{n+1} &= 2\eta_m^{n+\frac{1}{2}} - \eta_m^n. \end{aligned} \quad (4.6)$$

Here, $F_m^{n+\frac{1}{2}} = F_m(t^{n+\frac{1}{2}})$ for the implicit midpoint rule and $F_m^{n+\frac{1}{2}} = \frac{1}{2}(F_m(t^n) + F_m(t^{n+1}))$ for the Crank-Nicolson scheme.

Note that only the third equation requires the solution of a linear system to determine $\eta_m^{n+\frac{1}{2}}$. The involved matrix $M_m + \frac{\tau^2}{4}S_m$ is time-independent and rather low-dimensional (corresponding to the number of degrees of freedom of V_H). Therefore, the LU decomposition of this matrix can be computed once and stored, such that the whole time stepping procedure is very cheap.

Interpolation operator. As seen above, the interpolation operator in the LOD method is not merely a theoretical tool, but an integral part of the construction. In general, we assume that $I_H : H_0^1(\Omega) \rightarrow V_H$ is a projection, i.e., $I_H \circ I_H = I_H$. (Deviations are possible, but it facilitates the analysis). Furthermore, stability and approximation properties are required, which can be summarized in the low-contrast case as

$$\|v - I_H v\|_{L^2(K)} + H \|\nabla I_H v\|_{L^2(K)} \leq C_I H \|\nabla v\|_{L^2(U_1(K))}$$

for all $v \in H_0^1(\Omega)$ and all $K \in \mathcal{T}_H$. Several choices for I_H are possible and we refer to, e.g., [20] for a detailed discussion. For instance, [1] uses the L^2 projection. Another admissible and popular choice that we also used in our simulations is $I_H = E_H \circ \Pi_H$, where Π_H is the element-wise L^2 -projection onto $Q_1(\mathcal{T}_H)$. Moreover, E_H denotes an averaging operator, characterized for any $v_H \in Q_1(\mathcal{T}_H)$ and any vertex z of \mathcal{T}_H by

$$(E_H(v_H))(z) = \sum_{K \in \mathcal{T}_H : z \in K} (v_H|_K)(z) \cdot \frac{1}{\text{card}\{K' \in \mathcal{T}_H : z \in K'\}}.$$

In the high-contrast case, we require the above stability and approximation properties in norms weighted with a_ϵ . Precisely, for the analysis below, the interpolation operator I_H has to satisfy

$$\|\sqrt{a_\epsilon} \nabla I_H v\|_{L^2(K)} \leq C_I \|\sqrt{a_\epsilon} \nabla v\|_{L^2(U_1(K))} \quad \text{and} \quad \|\sqrt{a_\epsilon} w\|_{L^2(K)} \leq C_I H \|\sqrt{a_\epsilon} \nabla w\|_{L^2(U_1(K))} \quad (4.7)$$

for all $v \in H_0^1(\Omega)$, all $w \in W_h$ and all $K \in \mathcal{T}_H$. These conditions have been verified under certain geometric conditions on Ω_ϵ using special a_ϵ -weighted interpolation operators. For instance, [25] uses a_ϵ weighted L^2 -projections onto V_H on patches $\omega_z = \{K \in \mathcal{T}_H : z \in K\}$ and evaluates these interpolations at all vertices z to define $(I_H(v))(z)$. Assumption (4.7) is shown to hold if a_ϵ is quasi-monotone. This is for instance satisfied in the two-dimensional periodic case described in Section 3 above. For details, we refer to [25]. The geometric conditions for the Scott-Zhang-type interpolation in [15] are not so easy to describe, but examples mentioned therein include the periodic set-up of Ω_ϵ . In our numerical experiments, we use the following interpolation operator. We set $I_H = E_H \circ \Pi_{H,a}$, where $\Pi_{H,a}$ is the a_ϵ weighted element-wise L^2 -projection onto $Q_1(\mathcal{T}_H)$. Precisely, for any $v \in H^1(K)$, $\Pi_{H,a}(v) \in Q_1(K)$ is given by

$$\int_K a_\epsilon \Pi_{H,a}(v) \psi_H dx = \int_K a_\epsilon v \psi_H dx \quad \text{for all } \psi_H \in Q_1(K).$$

We note that, for this choice, (4.7) has not been proved to the best of our knowledge, but the results of [25] and of [9] concerning weighted projections indicate a validity of (4.7) in this case. In the following analysis we do not require the explicit form of I_H , but only use (4.7).

4.2 Error analysis for high-contrast media

We are interested in transferring the a priori error results in [1] to the present high-contrast setting. In order to have ϵ -explicit estimates, we have to carefully take into account any dependence on the contrast (i.e., the lower bound of a_ϵ). We write \lesssim to denote inequality up to a

multiplicative constant C , which does not depend on ϵ or the discretization parameters H, h and m . Note that the constants may depend on the final time T .

We will analyze errors for the semi-discrete method (4.3). Estimates for the full discretization can then be deduced following [1]. For the error analysis we require the following two assumptions.

Assumption 4.1. (a) The geometry of Ω_ϵ is such that an interpolation operator I_H satisfying (4.7) exists. Further, we assume that this I_H is used in the construction of the LOD.
(b) The geometry of Ω_ϵ is such that the following weighted Poincaré inequality holds: For all $v \in H_0^1(\Omega)$, there exists a constant C_P independent of ϵ such that

$$\|v\|_{L^2(\Omega)} \leq C_P \|\sqrt{a_\epsilon} \nabla v\|_{L^2(\Omega)}. \quad (4.8)$$

In the previous section, we already discussed the first part of the assumption. The weighted Poincaré inequality in the second part holds in the periodic case with compact inclusions, cf. [3, Rem. 4.2].

Ritz projection errors. As usual, we start with estimating the error of the elliptic (Ritz) projection $\pi_{H,m}^{ms}$ onto $V_{H,m}^{ms}$. In [15, 25], the following *contrast-independent* estimate for the truncation of the correctors is shown.

Lemma 4.2. *There exists a generic constant $0 < \gamma < 1$ (independent of H, h and ϵ) such that for any $v_H \in V_H$*

$$\|\sqrt{a_\epsilon} \nabla (\mathcal{C}_{h,m} - \mathcal{C}_{h,\Omega})(v_H)\|_{L^2(\Omega)} \lesssim m^{d/2} \gamma^m \|\sqrt{a_\epsilon} \nabla v_H\|_{L^2(\Omega)} \quad (4.9)$$

In the following, π_h denotes the (elliptic) Ritz projection onto the fine finite FE space V_h . The next lemma gives the error estimates for $\pi_{H,m}^{ms}$ in various norms.

Lemma 4.3. *The following estimates hold for almost every $t \in [0, T]$.*

(a) *For any $v \in L^1(H^1)$, we have*

$$\|\sqrt{a_\epsilon} (v(\cdot, t) - \pi_{H,m}^{ms} v(\cdot, t))\|_{L^2(\Omega)} \lesssim \|\sqrt{a_\epsilon} (v(\cdot, t) - \pi_h v(\cdot, t))\|_{L^2(\Omega)} + (H + m^{d/2} \gamma^m) \|\sqrt{a_\epsilon} \nabla v(\cdot, t)\|_{L^2(\Omega)}. \quad (4.10)$$

(b) *For the solution u_ϵ to (2.3) assume that $\partial_t^i u_\epsilon \in L^1(H_0^1)$ and $\partial_t^{2+i} u_\epsilon, \partial_t^i f \in L^1(L^2)$ for $i \in \{0, 1, 2\}$. Then,*

$$\|\sqrt{a_\epsilon} \nabla (\partial_t^i u_\epsilon(\cdot, t) - \pi_{H,m}^{ms} (\partial_t^i u_\epsilon(\cdot, t)))\|_{L^2(\Omega)} \quad (4.11)$$

$$\lesssim \|\sqrt{a_\epsilon} \nabla (\partial_t^i u_\epsilon(\cdot, t) - \pi_h (\partial_t^i u_\epsilon(\cdot, t)))\|_{L^2(\Omega)} + (H + m^{d/2} \gamma^m) (\|(a_\epsilon)^{-1/2} (\partial_t^{i+2} u_\epsilon - \partial_t^i f)\|_{L^2(\Omega)} + \|\sqrt{a_\epsilon} \nabla \partial_t^i u_\epsilon\|_{L^2(\Omega)}),$$

$$\|\partial_t^i u_\epsilon(\cdot, t) - \pi_{H,m}^{ms} (\partial_t^i u_\epsilon(\cdot, t))\|_{L^2(\Omega)} \quad (4.12)$$

$$\lesssim \|\partial_t^i u_\epsilon(\cdot, t) - \pi_h (\partial_t^i u_\epsilon(\cdot, t))\|_{L^2(\Omega)} + (H + m^{d/2} \gamma^m) (\|(a_\epsilon)^{-1/2} (\partial_t^{i+2} u_\epsilon - \partial_t^i f)\|_{L^2(\Omega)} + \|\sqrt{a_\epsilon} \nabla \partial_t^i u_\epsilon\|_{L^2(\Omega)}).$$

Proof. For simplicity, we will omit time dependencies throughout the proof if no confusion can arise.

Proof of (4.10): Let $e_{H,m} = \pi_{H,m}^{ms} v - \pi_h v$. We introduce the dual solution $z \in H_0^1(\Omega)$ such that

$$b_\epsilon(\psi, z) = (e_{H,m}, \psi)_a.$$

Note that it holds

$$\|\sqrt{a_\epsilon} \nabla z\|_{L^2(\Omega)} \lesssim \|\sqrt{a_\epsilon} e_{H,m}\|_{L^2(\Omega)}$$

by standard elliptic a priori (stability) estimates using (4.8). Then we obtain

$$\begin{aligned} \|e_{H,m}\|_{L^2_a(\Omega)}^2 &= b_\epsilon(e_{H,m}, z) = b_\epsilon(e_{H,m}, z - z_{H,m}) \\ &\lesssim \|\sqrt{a_\epsilon} \nabla e_{H,m}\|_{L^2(\Omega)} \|\sqrt{a_\epsilon} \nabla (z - z_{H,m})\|_{L^2(\Omega)} \end{aligned}$$

for any $z_{H,m} \in V_{H,m}^{ms}$. We choose $z_{H,m} = (1 + \mathcal{C}_{h,m})I_H z = (1 + \mathcal{C}_{h,\Omega})z + (\mathcal{C}_{h,m} - \mathcal{C}_{h,\Omega})I_H z$. Because of (4.9) and (4.7), we deduce for the second term

$$\|\sqrt{a_\epsilon} \nabla (\mathcal{C}_{h,m} - \mathcal{C}_{h,\Omega})I_H z\|_{L^2(\Omega)} \lesssim m^{d/2} \gamma^m \|\sqrt{a_\epsilon} \nabla z\|_{L^2(\Omega)} \lesssim m^{d/2} \gamma^m \|\sqrt{a_\epsilon} e_{H,m}\|_{L^2(\Omega)},$$

where we used the a priori (stability) estimate for z in the last step. For the first term $z - (1 + \mathcal{C}_{h,\Omega})z = -\mathcal{C}_{h,\Omega}z$ we obtain

$$\begin{aligned} \|\sqrt{a_\epsilon} \nabla \mathcal{C}_{h,\Omega}z\|_{L^2(\Omega)}^2 &\leq b_\epsilon(\mathcal{C}_{h,\Omega}z, \mathcal{C}_{h,\Omega}z) = b_\epsilon(\mathcal{C}_{h,\Omega}z, z) = (e_{H,m}, \mathcal{C}_{h,\Omega}z)_a \\ &\leq \|\sqrt{a_\epsilon} e_{H,m}\|_{L^2(\Omega)} \|\sqrt{a_\epsilon} \mathcal{C}_{h,\Omega}z\|_{L^2(\Omega)} \\ &\lesssim H \|\sqrt{a_\epsilon} e_{H,m}\|_{L^2(\Omega)} \|\sqrt{a_\epsilon} \nabla \mathcal{C}_{h,\Omega}z\|_{L^2(\Omega)}, \end{aligned}$$

where we used $\mathcal{C}_{h,\Omega}z \in W_h$ and (4.7) in the last step. Collecting the results, we have shown that

$$\|\sqrt{a_\epsilon} e_{H,m}\|_{L^2(\Omega)} \lesssim (H + m^{d/2} \gamma^m) \|\sqrt{a_\epsilon} \nabla e_{H,m}\|.$$

The stability of the Ritz projections $\pi_{H,m}^{ms}$ and π_h as well as the triangle inequality finish the proof of (4.10).

Proof of (4.11): Introduce the simplified notation $v_\epsilon = \partial_{tt}^i u_\epsilon$ and $\bar{f} = \partial_{tt}^i f$. Observe that v_ϵ solves

$$(\partial_{tt} v_\epsilon(\cdot, t), \psi) + b_\epsilon(v_\epsilon(\cdot, t), \psi) = (\bar{f}(\cdot, t), \psi) \quad \forall \psi \in H_0^1(\Omega).$$

By the definition of the Ritz projections, we see that

$$\|\sqrt{a_\epsilon} \nabla (\pi_h v_\epsilon - \pi_{H,m}^{ms} v_\epsilon)\|_{L^2(\Omega)} \leq \inf_{v_{H,m} \in V_{H,m}^{ms}} \|\sqrt{a_\epsilon} \nabla (\pi_h v - v_{H,m}^{ms})\|_{L^2(\Omega)}.$$

As in the previous step, we choose $v_{H,m} = (1 + \mathcal{C}_{h,m})I_H \pi_h v_\epsilon$ and estimate

$$\begin{aligned} \|\sqrt{a_\epsilon} \nabla (\pi_{H,m}^{ms} v_\epsilon - \pi_h v_\epsilon)\|_{L^2(\Omega)} &\leq \|\sqrt{a_\epsilon} \nabla \mathcal{C}_{h,\Omega} \pi_h v_\epsilon\|_{L^2(\Omega)} + \|\sqrt{a_\epsilon} \nabla (\mathcal{C}_{h,m} - \mathcal{C}_{h,\Omega}) \pi_h v_\epsilon\|_{L^2(\Omega)} \\ &\lesssim \|\sqrt{a_\epsilon} \nabla \mathcal{C}_{h,\Omega} \pi_h v_\epsilon\|_{L^2(\Omega)} + m^{d/2} \gamma^m \|\sqrt{a_\epsilon} \nabla v_\epsilon\|_{L^2(\Omega)}, \end{aligned}$$

where we used (4.9) and the stability of π_h in the last step. For $\mathcal{C}_{h,\Omega} \pi_h v_\epsilon$ we obtain with the definition of $\mathcal{C}_{h,\Omega}$ and π_h that

$$\begin{aligned} \|\sqrt{a_\epsilon} \nabla \mathcal{C}_{h,\Omega} \pi_h v_\epsilon\|_{L^2(\Omega)}^2 &\leq b_\epsilon(\mathcal{C}_{h,\Omega} \pi_h v_\epsilon, \mathcal{C}_{h,\Omega} \pi_h v_\epsilon) = b_\epsilon(v_\epsilon, \mathcal{C}_{h,\Omega} \pi_h v_\epsilon) \\ &= (\bar{f} - \partial_{tt} v_\epsilon, \mathcal{C}_{h,\Omega} \pi_h v_\epsilon - I_H \mathcal{C}_{h,\Omega} \pi_h v_\epsilon)_{L^2(\Omega)} \\ &\lesssim H \|(a_\epsilon)^{-1/2} (\bar{f} - \partial_{tt} v_\epsilon)\|_{L^2(\Omega)} \|\sqrt{a_\epsilon} \nabla \mathcal{C}_{h,\Omega} \pi_h v_\epsilon\|_{L^2(\Omega)}, \end{aligned}$$

where we employed (4.7) in the last step. Combination of the foregoing estimates and the triangle inequality yield the result.

Proof of (4.12): Follows from the weighted Poincaré inequality (4.8) and (4.11). \square

Note that we have the term $\|(a_\epsilon)^{-1/2} (\bar{f} - \partial_{tt} v_\epsilon)\|_{L^2(\Omega)}$ on the right-hand side of (4.11)–(4.12) because the application of (4.7) to $\mathcal{C}_{h,\Omega} \pi_h v_\epsilon$ requires the weighted L^2 -norm. This agrees with the error estimates for stationary source problems, see, e.g., [26]. We discuss bounds on $\|(a_\epsilon)^{-1/2} (\bar{f} - \partial_{tt} v_\epsilon)\|_{L^2(\Omega)}$ in Remark 4.5. By combining the proof for (4.10) with (4.11), we obtain a quadratic rate for the Ritz projection error of v_ϵ in the weighted L^2 -norm. This bound is, however, not needed in our main arguments below.

Semi-discrete error analysis. We employ the usual splitting of $u - u_{H,m}^{ms}$ into the Ritz projection error $\rho = u - \pi_{H,m}^{ms} u$, for which we can apply Lemma 4.3, and the remainder term $\eta = \pi_{H,m}^{ms} u - u_{H,m}^{ms}$, which belongs to the finite-dimensional space $V_{H,m}^{ms}$.

Theorem 4.4. (a) Assume that $\partial_t^3 u_\epsilon, \partial_t f \in L^\infty(L^2)$, $\partial_t^4 u_\epsilon, \partial_{tt} f \in L^1(L^2)$, $\partial_t u_\epsilon \in L^\infty(H_0^1)$ and $\partial_{tt} u_\epsilon \in L^1(H_0^1)$. If we choose $v_{H,m}^0 = \pi_{H,m}^{ms}(v^0)$ in (4.3), then

$$\begin{aligned} & \|\partial_t u_\epsilon - \partial_t u_{H,m}^{ms}\|_{L^\infty(L^2)} + \|\sqrt{a_\epsilon} \nabla (u_\epsilon - u_{H,m}^{ms})\|_{L^\infty(L^2)} \\ & \lesssim (H + m^{d/2} \gamma^m) \left(\sum_{i=0}^1 \|(a_\epsilon)^{-1/2} (\partial_t^{i+2} u_\epsilon - \partial_t^i f)\|_{L^\infty(L^2)} + \|(a_\epsilon)^{-1/2} (\partial_t^4 u_\epsilon - \partial_{tt} f)\|_{L^1(L^2)} \right) \\ & \quad + \sum_{i=0}^1 \|\sqrt{a_\epsilon} \nabla \partial_t u_\epsilon\|_{L^\infty(L^2)} + \|\sqrt{a_\epsilon} \nabla \partial_{tt} u_\epsilon\|_{L^1(L^2)} + e_{\text{disc}}^1(h) \end{aligned} \quad (4.13)$$

with the fine-scale discretization error

$$e_{\text{disc}}^1(h) = \|(1 - \pi_h) \partial_t u_\epsilon\|_{L^\infty(L^2)} + \|\sqrt{a_\epsilon} \nabla (1 - \pi_h) u_\epsilon\|_{L^\infty(L^2)} + \|(1 - \pi_h) \partial_{tt} u_\epsilon\|_{L^\infty(L^2)}.$$

(b) Assume that $\partial_{tt} u_\epsilon \in L^\infty(L^2)$, $\partial_t^3 u_\epsilon, \partial_t f \in L^1(L^2)$, and $\partial_t u_\epsilon \in L^1(H_0^1)$, then

$$\begin{aligned} & \|u_\epsilon - u_{H,m}^{ms}\|_{L^\infty(L^2)} \\ & \lesssim (H + m^{d/2} \gamma^m) \left(\|(a_\epsilon)^{-1/2} (\partial_{tt} u_\epsilon - f)\|_{L^\infty(L^2)} + \|(a_\epsilon)^{-1/2} (\partial_t^3 u_\epsilon - \partial_t f)\|_{L^1(L^2)} \right) \\ & \quad + \|\sqrt{a_\epsilon} \nabla u_\epsilon\|_{L^\infty(L^2)} + \|\sqrt{a_\epsilon} \nabla \partial_t u_\epsilon\|_{L^1(L^2)} + e_{\text{disc}}^2(h), \end{aligned} \quad (4.14)$$

with the fine-scale discretization error $e_{\text{disc}}^2(h) = \|(1 - \pi_h) u_\epsilon\|_{L^\infty(L^2)} + \|(1 - \pi_h) \partial_t u_\epsilon\|_{L^1(L^2)}$.

Remark 4.5 (Estimating the right-hand side of (4.13)–(4.14)). With respect to the ϵ -dependency, the most critical terms in (4.13)–(4.14) are the first two terms each as they are weighted with $(a_\epsilon)^{-1/2} \sim \epsilon^{-1}$. From the consideration of source problems, cf. [26], we expect the term $(a_\epsilon)^{-1/2} f$. Note that the critical ϵ -dependency vanishes if f has support outside Ω_ϵ . For the Helmholtz problem, [26] further discusses that the occurrence $(a_\epsilon)^{-1/2} f$ in the error estimates can be interpreted in the light of homogenization theory. To estimate the terms $(a_\epsilon)^{-1/2} \partial_t^i u_\epsilon$ in (4.13)–(4.14), we bound $(a_\epsilon)^{-1/2}$ by ϵ^{-1} and use (time-)regularity estimates following from [1, Prop. 4.4] and [11, Ch. 7.2]. Compactly written, one obtains for $i \in \mathbb{N}_0$ that

$$\|(a_\epsilon)^{-1/2} \partial_t^{i+1} u_\epsilon\|_{L^\infty(L^2)} \lesssim_T \epsilon^{-1} (\|\partial_t^i f\|_{L^2(L^2)} + \|w_i\|_{H^1(\Omega)} + \|w_{i+1}\|_{L^2(\Omega)}),$$

where w_i is inductively defined via $w_0 = u^0$, $w_1 = v^0$ and $w_i = \partial_t^i f(\cdot, 0) + \nabla \cdot (a_\epsilon \nabla w_{i-1}(\cdot, 0))$ for $i \geq 2$. In particular, for zero initial data and if time derivatives of f are zero at $t = 0$, the terms w_i vanish and the time regularity estimate is left with $\epsilon^{-1} \|\partial_t^i f\|_{L^2(L^2)}$ on the right-hand side. Such an ϵ -dependency in front of f also shows up from our previous discussion of the source problem if f has some support in Ω_ϵ .

Note that similar time regularity estimates also allow to bound the third and fourth term in (4.13)–(4.14) each. Since the ϵ -dependency for these terms is not critical, we, however, do not discuss them in further detail.

Summarizing, we can further estimate (4.13)–(4.14) using time regularity estimates similar as in [1]. In particular, the required time regularity of u_ϵ can be achieved for so-called compatible initial data, i.e., if w_i up to the required index i exist and lie in the necessary spaces $H_0^1(\Omega)$ or $L^2(\Omega)$, cf. [1] for precise statements. However, such compatible initial data may still induce (critical) ϵ -dependencies on the right-hand side in our high-contrast case. Completely ϵ -independent bounds can be achieved if the initial data as well as $\partial_t^i f(\cdot, 0)$ are zero and if f (and its time derivatives) have a small (i.e., $O(\epsilon)$) L^2 -norm.

Remark 4.6 (Error estimates in weighted L^2 -norm). In view of the Ritz projection estimate (4.10), one might aim for error estimates in the weighted L^2 -norm with the hope to avoid the critical terms $(a_\epsilon)^{-1/2} \partial_t^i u_\epsilon$ discussed in the previous remark. Unfortunately, we are not aware of standard energy techniques that allow for such estimates. In the stationary case, one typically uses dual problems and the Aubin-Nitsche trick, but this also does not appear to be possible in the wave setting to the best of our knowledge.

Therefore, we can only conjecture the following estimate

$$\|\sqrt{a_\epsilon}(u - u_{H,m}^{ms})\|_{L^\infty(L^2)} \lesssim_T \|\sqrt{a_\epsilon}(1 - \pi_h) \partial_t u_\epsilon\|_{L^1(L^2)} + (H + m^{d/2} \gamma^m) \|\sqrt{a_\epsilon} \nabla \partial_t u_\epsilon\|_{L^1(L^2)}.$$

By differentiating (2.3) with respect to time, we can get the time regularity estimate

$$\|\sqrt{a_\epsilon} \nabla \partial_t u_\epsilon\|_{L^1(L^2)} \lesssim_T \|\partial_t f\|_{L^2(L^2)} + \|v^0\|_{H^1(\Omega)} + \|w_2\|_{L^2(\Omega)}$$

with $w_2 = f(\cdot, 0) + \nabla \cdot (a_\epsilon \nabla u^0)$ as in the previous remark. If $\|w_2\|_{L^2(\Omega)}$ is bounded independent of ϵ , which is for instance the case for $u^0 = 0$ and f independent of ϵ , this implies an ϵ -independent error estimate in the weighted L^2 -norm as conjecture.

Proof of Theorem 4.4. Proof of (4.13): Following [18], we split $u - u_{H,m}^{ms} = \rho + \eta$ as already discussed. We directly obtain that

$$(\partial_{tt} \eta, \psi) + b_\epsilon(\theta, \psi) = -(\partial_{tt} \rho, \psi) \quad \forall \psi \in V_{H,m}^{ms}. \quad (4.15)$$

Testing with $\psi = \partial_t \eta$, we deduce

$$\frac{d}{dt} (\|\partial_t \eta\|_{L^2(\Omega)}^2 + \|\sqrt{a_\epsilon} \nabla \eta\|_{L^2(\Omega)}^2) \leq \|\partial_{tt} \rho\|_{L^2(\Omega)}^2 + \|\partial_t \eta\|_{L^2(\Omega)}^2.$$

Application of Gronwall's inequality yields

$$\|\partial_t \eta\|_{L^\infty(L^2)} + \|\sqrt{a_\epsilon} \nabla \eta\|_{L^\infty(L^2)} \lesssim_T \|\partial_t \eta(\cdot, 0)\|_{L^2(\Omega)} + \|\sqrt{a_\epsilon} \nabla \eta(\cdot, 0)\|_{L^2(\Omega)} + \|\partial_{tt} \rho\|_{L^1(0,T;L^2(\Omega))}.$$

The term $\|\partial_{tt} \rho\|_{L^1(0,T;L^2(\Omega))}$ can be treated with (4.12). By the choice of the initial values, we have $\eta(\cdot, 0) = 0$ and $\partial_t \eta(\cdot, 0) = 0$. Combination with (4.11)–(4.12) finishes the proof of (4.13).

Proof of (4.14): As in [6], we re-write (4.15) as

$$\frac{d}{dt} (\partial_t \eta, \psi) - (\partial_t \eta, \partial_t \psi) + b_\epsilon(\eta, \psi) = -\frac{d}{dt} (\partial_t \rho, \psi) + (\partial_t \rho, \partial_t \psi) \quad \forall \psi \in L^1(0, T; V_{H,m}^{ms}).$$

Fixing some $0 < t_0 < T$, we choose $\psi(\cdot, t) = \int_t^{t_0} \eta(\cdot, s) ds$ and observe that $\partial_t \psi = -\eta$. This gives

$$\frac{1}{2} \frac{d}{dt} \|\eta(\cdot, t)\|_{L^2(\Omega)}^2 - \frac{1}{2} \frac{d}{dt} b_\epsilon \left(\int_t^{t_0} \eta, \int_t^{t_0} \eta \right) = -\frac{d}{dt} \left(\partial_t (u - u_{H,m}^{ms}), \int_t^{t_0} \eta \right) - (\partial_t \rho, \eta).$$

Integration from 0 to t_0 yields

$$\begin{aligned} \|\eta(\cdot, t_0)\|_{L^2(\Omega)}^2 &\leq \|\eta(\cdot, 0)\|_{L^2(\Omega)}^2 + \left(\partial_t (u - u_{H,m}^{ms})(\cdot, 0), \int_0^{t_0} \eta \right) - \int_0^{t_0} (\partial_t \rho, \eta) \\ &\leq \|\eta(\cdot, 0)\|_{L^2(\Omega)}^2 + 2\|\partial_t \rho\|_{L^1(L^2)}^2 + \frac{1}{2} \|\eta\|_{L^\infty(L^2)}^2. \end{aligned}$$

In the second step we used $\partial_t (u - u_{H,m}^{ms})(\cdot, 0) = v^0 - P_{H,m}^{ms} v^0$ and $\eta \in V_{H,m}^{ms}$. Taking the maximum over $0 < t_0 < T$, we arrive at

$$\|\eta\|_{L^\infty(L^2)}^2 \lesssim \|\eta(\cdot, 0)\|_{L^2(\Omega)}^2 + \|\partial_t \rho\|_{L^1(L^2)}^2$$

The last term can be estimated with (4.12) and, as in the previous step, we have $\eta(\cdot, 0) = 0$. \square

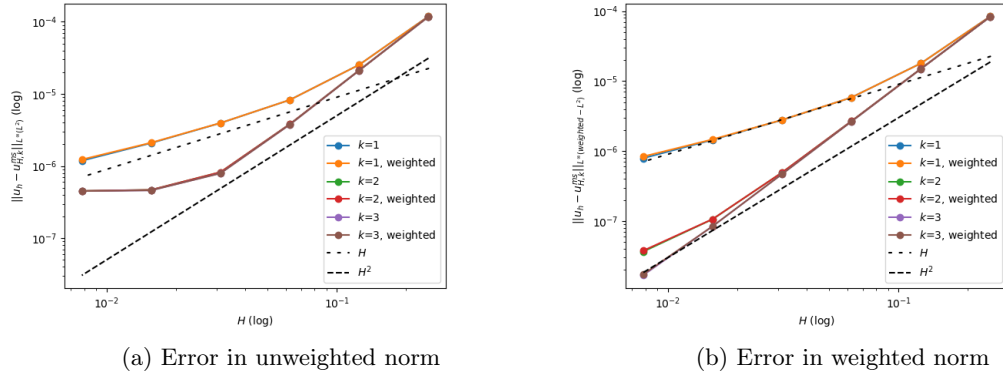


Figure 4.1: Error convergence for the one-dimensional periodic setting with $f = x(x - 1)$

4.3 Numerical illustrations

In this section, we illustrate the theoretical convergence rates with numerical experiments in one and two dimensions. The implementation is based on the `python`-module `gridlod` [14] and the Petrov-Galerkin formulation of the LOD method. We always choose $\Omega = (0, 1)^d$ and $T = 0.25$ as well as $u^0 = v^0 = 0$. We consider different right-hand sides, which are specified in each numerical experiment. This set-up of zero initial values seems attractive from the viewpoint of “compatible” data and time regularity estimates as discussed in Remark 4.5. Furthermore, it ensures that we are not in the “simple” case of Proposition 3.1 in the one-dimensional case. In our experiments, we will consider periodic high-contrast a_ϵ as in the numerical simulations of Section 3.3 and a random checkerboard realization (with high contrast) for a_ϵ . The latter is generated as follows: On a subdivision of Ω into cuboids of side length ϵ , a_ϵ is piecewise constant and the value of a_ϵ in each cuboid is chosen as 1 or ϵ^2 with probability 0.5 (independently for all cuboids). All the plots below show $L^\infty(L^2)$ or $L^\infty(L^2_a)$ -errors between a reference solution and the time-discretized version of $u_{H,m} \in V_{H,m}^{ms}$, whose vector of degrees of freedom at time t^n is given by ζ_m^n from (4.6), using the implicit midpoint rule. Here, L^2_a denotes the usual L^2 -space but with the a_ϵ -weighted norm $\|\sqrt{a_\epsilon} \cdot\|_{L^2(\Omega)}$.

One-dimensional case. We choose $\epsilon = 2^{-10}$ and compute a reference solution using the mesh size $h = 2^{-13}$, which clearly resolves the variations of a_ϵ , and a time step $\tau = 2^{-9}$. First, we consider the periodic set-up with $f = x(x - 1) \in H_0^1(\Omega)$. For the series of LOD discretization parameters $k = 1, 2, 3$ and $H = 2^{-2}, \dots, 2^{-7}$, Figure 4.1 shows the errors in the two discussed norms, namely $L^\infty(L^2)$ and $L^\infty(L^2_a)$. Further, we compare the use of the standard interpolation operator I_H and its weighted version (cf. the discussion in Section 4.1). Except for the case $k = 1$, we observe a quadratic convergence rate in both norms and irrespective of the chosen interpolation operator. This higher rate in comparison to Theorem 4.4 and (conjectured) Remark 4.6 is related to higher spatial regularity. While the convergence rates are roughly similar for both norms, the errors in the weighted L^2 -norm are clearly smaller and, additionally, the convergence does not slow down for finer mesh sizes H . The latter effect may be related to a stronger ϵ -dependency in the L^2 -error estimate as discussed in Remarks 4.5 and 4.6.

Next, we study the random realization of a_ϵ . As expected or conjectured, we observe linear convergence in both weighted and unweighted L^2 -norms, see Figure 4.2. This underlines the applicability of the method beyond the periodic case. Note that for both choices of a_ϵ , the choice of I_H does not have a great influence on the observed errors in the target regime of large H .

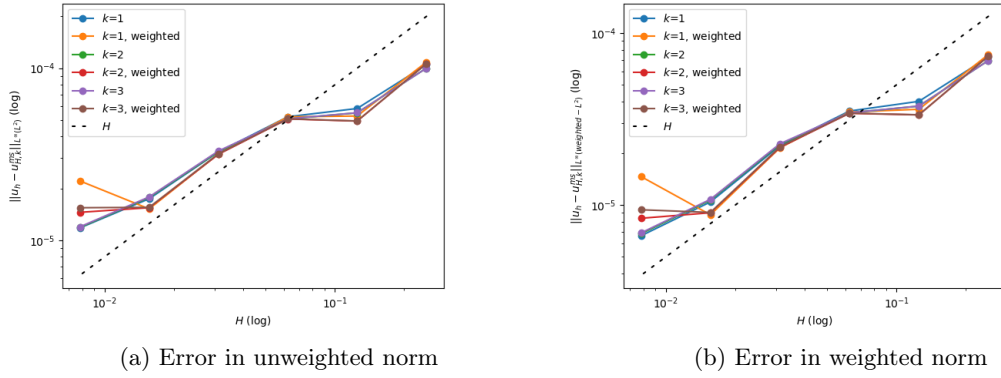


Figure 4.2: Error convergence for the one-dimensional random setting with $f = x(x - 1)$

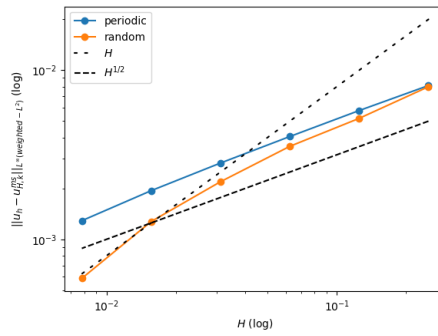
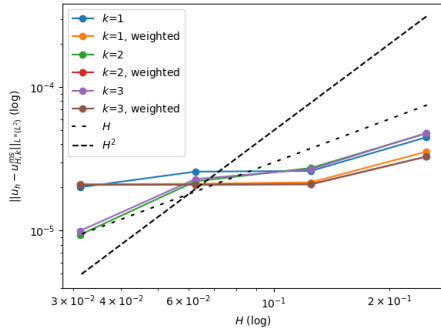


Figure 4.3: Error convergence for the one-dimensional setting with $f = 1$

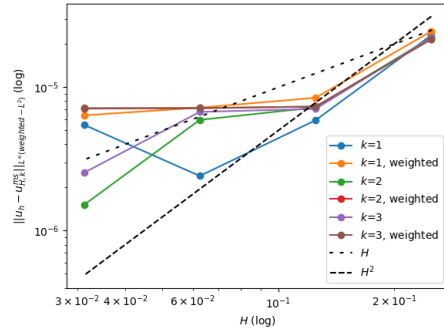
Finally, we briefly consider $f \equiv 1$. Discussions in [20] for the stationary problem indicate that regularity of f may lead to higher convergence rates only if f also satisfies the zero boundary conditions. We focus on the case $k = 3$ and the weighted L^2 -norm. Since we previously did not observe an impact of the interpolation operator, we only depict results for the unweighted interpolation operator, but we confirmed our observations also for the weighted variant of I_H . Figure 4.3 shows a similar convergence rate for the periodic and the random case, which lies somewhere between 0.5 and the (conjectured) 1. The reduction in the convergence rate possibly is due to less compatible data and therefore less regularity and/or more critical ϵ factors in the estimates.

Two-dimensional case. In the two-dimensional setting, we choose $\epsilon = 2^{-5}$ and compute the reference solution with mesh size $h = 2^{-7}$ and $\tau = 2^{-9}$. The LOD discretization parameters are varied as $k = 1, 2, 3$ and $H = 2^{-2}, \dots, 2^{-5}$. Results for the periodic setting with $f = x_1 x_2 (x_1 - 1)(x_2 - 1) \in H_0^1(\Omega)$ are depicted in Figure 4.4. In the two-dimensional setting, the different norms also show different error behavior. More than linear convergence seems to be achievable for the weighted L^2 -norm overall, but at most linear convergence is observed in the standard L^2 -norm. The choice of the interpolation operator now has a larger impact and, interestingly, the unweighted variant gives the better results in this experiment.

As most demanding test case, we consider the random checkerboard in two dimensions. We set a_ϵ as described in the beginning, but only in the inner domain $(0.25, 0.75)^2$, outside we set

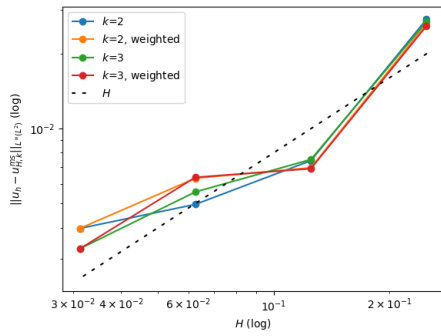


(a) Error in unweighted norm

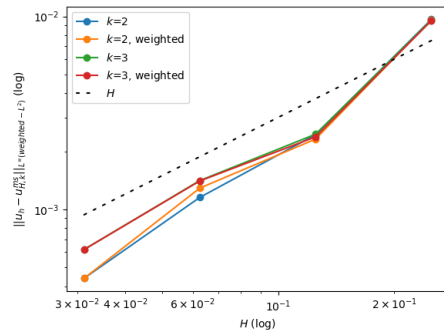


(b) Error in weighted norm

Figure 4.4: Error convergence for the two-dimensional periodic setting



(a) Error in unweighted norm



(b) Error in weighted norm

Figure 4.5: Error convergence for the two-dimensional random setting

it equal to 1. This set-up is to prevent small values of a_ϵ close to the boundary. In the light of our discussion of the ϵ -dependency of our error estimates, we choose f in such a way that its support does not intersect with Ω_ϵ . Here, we set $f = 1$ in $\Omega \setminus (0.25, 0.75)^2$ and zero elsewhere. Despite the low regularity of f , the errors in Figure 4.5 converge nicely, in particular we observe the conjectured linear convergence in the weighted L^2 -norm. We omitted the results for $k = 1$ here, since the localization/truncation error is dominating and the errors therefore do not decay.

Overall, the two-dimensional results show expected or conjectured convergence rates, especially for the weighted L^2 -norm, which seems to be the best choice in the high-contrast setting. Moreover, our numerical experiments underline the practicability of the LOD method even for very unstructured high-contrast coefficients. The influence of the interpolation operator needs to be further investigated in the high-contrast case – both theoretically as well as numerically.

Conclusion

We discussed wave propagation in high-contrast media, where the lower bound of the material coefficient is coupled to the fine-scale parameter ϵ . Asymptotic analysis results in the periodic case underline the difference between low- and high-contrast settings. In particular, we could show a new result in one space dimension, where the limit solution takes a simple form. Numerical simulations illustrated these findings and the special role of the one-dimensional setting.

To cope with more general high contrast coefficients, we reviewed the Localized Orthogonal Decomposition method for the wave equation. We showed rigorous a priori error estimates in the semi-discrete setting and especially discussed the dependence on the high contrast. Several numerical experiments illustrated our findings and showed the potential of the method. Open questions for future work concern (i) the error estimate in a weighted L^2 -norm, which seems to have practical relevance in view of our numerical tests, and (ii) the selection of the interpolation operator. In the periodic setting, a better understanding of the homogenization limit and its numerical tractability in higher dimensions is desirable as well. Overall our results clearly indicate the need for a better understanding of wave propagation in high-contrast media and that a lot of interesting effects are to be expected in the future. For instance, we did not search for resonance phenomena similar to those in the time-harmonic regime [26].

References

- [1] A. Abdulle and P. Henning. Localized orthogonal decomposition method for the wave equation with a continuum of scales. *Math. Comp.*, 86(304):549–587, 2017.
- [2] A. Abdulle and P. Henning. Multiscale methods for wave problems in heterogeneous media. In *Handbook of numerical methods for hyperbolic problems*, volume 18 of *Handb. Numer. Anal.*, pages 545–576. Elsevier/North-Holland, Amsterdam, 2017.
- [3] G. Allaire. Homogenization and two-scale convergence. *SIAM J. Math. Anal.*, 23(6):1482–1518, 1992.
- [4] R. Altmann, P. Henning, and D. Peterseim. Numerical homogenization beyond scale separation. *Acta Numer.*, 30:1–86, 2021.
- [5] H. Ammari, B. Davies, E. O. Hiltunen, H. Lee, and S. Yu. Wave interaction with subwavelength resonators. In *Applied mathematical problems in geophysics*, volume 2308 of *Lecture Notes in Math.*, pages 23–83. Springer, Cham, 2022.
- [6] G. A. Baker. Error estimates for finite element methods for second order hyperbolic equations. *SIAM J. Numer. Anal.*, 13(4):564–576, 1976.
- [7] A. Bensoussan, J.-L. Lions, and G. Papanicolaou. *Asymptotic analysis for periodic structures*, volume 5 of *Studies in Mathematics and its Applications*. North-Holland Publishing Co., Amsterdam-New York, 1978.
- [8] G. Bouchitté, C. Bourel, and D. Felbacq. Homogenization near resonances and artificial magnetism in three dimensional dielectric metamaterials. *Arch. Ration. Mech. Anal.*, 225(3):1233–1277, 2017.
- [9] J. H. Bramble and J. Xu. Some estimates for a weighted L^2 projection. *Math. Comp.*, 56(194):463–476, 1991.
- [10] M. Cherdantsev, K. Cherednichenko, and S. Cooper. Extreme localization of eigenfunctions to one-dimensional high-contrast periodic problems with a defect. *SIAM J. Math. Anal.*, 50(6):5825–5856, 2018.
- [11] L. C. Evans. *Partial differential equations*, volume 19 of *Graduate Studies in Mathematics*. American Mathematical Society, Providence, RI, second edition, 2010.

- [12] S. Geevers and R. Maier. Fast mass lumped multiscale wave propagation modelling. *IMA Journal of Numerical Analysis*, 2021.
- [13] T. Gustafsson and G. D. McBain. scikit-fem: A Python package for finite element assembly. *Journal of Open Source Software*, 5(52):2369, 2020.
- [14] F. Hellman and T. Keil. gridlod. GitHub repository. commit 0ed4c096df75040145978d48c5307ef5678efed3.
- [15] F. Hellman and A. Målqvist. Contrast independent localization of multiscale problems. *Multiscale Model. Simul.*, 15(4):1325–1355, 2017.
- [16] A. Lamacz and B. Schweizer. A negative index meta-material for Maxwell’s equations. *SIAM J. Math. Anal.*, 48(6):4155–4174, 2016.
- [17] A. Lamacz and B. Schweizer. Effective acoustic properties of a meta-material consisting of small Helmholtz resonators. *Discrete Contin. Dyn. Syst. Ser. S*, 10(4):815–835, 2017.
- [18] S. Larsson and V. Thomée. *Partial differential equations with numerical methods*, volume 45 of *Texts in Applied Mathematics*. Springer-Verlag, Berlin, 2003.
- [19] R. Maier and D. Peterseim. Explicit computational wave propagation in micro-heterogeneous media. *BIT*, 59(2):443–462, 2019.
- [20] A. Målqvist and D. Peterseim. *Numerical homogenization by localized orthogonal decomposition*, volume 5 of *SIAM Spotlights*. Society for Industrial and Applied Mathematics (SIAM), Philadelphia, PA, 2021.
- [21] A. Nandakumaran and A. Sili. Homogenization of a hyperbolic equation with highly contrasting diffusivity coefficients. *Differential Integral Equations*, 29(1/2):37–54, 2016.
- [22] M. Ohlberger, B. Schweizer, M. Urban, and B. Verfürth. Mathematical analysis of transmission properties of electromagnetic meta-materials. *Netw. Heterog. Media*, 15(1):29–56, 2020.
- [23] M. Ohlberger and B. Verfürth. A new heterogeneous multiscale method for the Helmholtz equation with high contrast. *Multiscale Model. Simul.*, 16(1):385–411, 2018.
- [24] H. Owhadi and L. Zhang. Numerical homogenization of the acoustic wave equations with a continuum of scales. *Comput. Methods Appl. Mech. Engrg.*, 198(3-4):397–406, 2008.
- [25] D. Peterseim and R. Scheichl. Robust numerical upscaling of elliptic multiscale problems at high contrast. *Comput. Methods Appl. Math.*, 16(4):579–603, 2016.
- [26] D. Peterseim and B. Verfürth. Computational high frequency scattering from high-contrast heterogeneous media. *Math. Comp.*, 89(326):2649–2674, 2020.
- [27] B. Schweizer. Resonance meets homogenization: construction of meta-materials with astonishing properties. *Jahresber. Dtsch. Math.-Ver.*, 119(1):31–51, 2017.
- [28] B. Verfürth. Heterogeneous multiscale method for the Maxwell equations with high contrast. *ESAIM Math. Model. Numer. Anal.*, 53(1):35–61, 2019.